

A Monte Carlo Study of strange particle production at NICA/MPD

Mariya Ilieva*, Vadim Kolesnikov, Dilyana Suvarieva, Veronica Vasendina and Alexander Zinchenko

*VBLHEP, Joint Institute for Nuclear Research,
141980 Dubna, Moscow region, Russia*

*E-mail: maia.ilieva@mail.bg, Vadim.Kolesnikov@cern.ch,
DilyanaSuvarieva@mail.bg, vasveron@mail.ru,
Alexander.Zinchenko@jinr.ru*

One of the main tasks of the NICA/MPD physics program is a study of the strangeness production in nuclear collisions. In this paper the MPD detector performance is presented for measurements of Λ , $\bar{\Lambda}$, Ξ^- , Ω^- -hyperons and hypertritons in central Au+Au collisions at NICA energies.

*XXII International Baldin Seminar on High Energy Physics Problems,
15-20 September 2014
JINR, Dubna, Russia*

*Speaker.

1. Introduction

The Nuclotron-based Ion Collider fAcility (NICA) [1] is a new accelerator complex being constructed at JINR, Dubna, Russia. NICA's aim is to provide collisions of heavy ions over a wide range of atomic masses, from Au+Au at $\sqrt{s} = 4 - 11$ A GeV (for Au⁷⁹⁺) and an average luminosity $L = 10^{27} \text{ cm}^{-2}\text{s}^{-1}$ to proton-proton collisions with $\sqrt{s_{pp}} = 20$ GeV and $L = 10^{32} \text{ cm}^{-2}\text{s}^{-1}$.

The main goal of studying heavy-ion collisions is to explore the properties of nuclear matter under extreme density and temperature conditions. The energy range of the NICA collider is ideal for an experimental exploration of fundamental QCD properties that are sensitive to such phenomena as deconfinement and chiral symmetry restoration [2].

Production of strange particles is of particular interest because enhanced production of rare strange hadrons (Ξ^- , Ω^-) in A+A collisions (relative to the yields from elementary pp reactions) was predicted as a signal for the Quark-Gluon Plasma (QGP) formation [3]. At present, a complete theoretical description of the (multi)strangeness production mechanism at collision energies (\sqrt{s}) of several GeV has not yet been achieved. In order to better understand the dynamics of hot and dense hadronic matter the MultiPurpose Detector (MPD) experiment at NICA [4] will provide new precise experimental data on the total yields, rapidity, transverse momentum, and azimuthal angle distributions of hyperons. The production of baryons and antibaryons with different strangeness content in central heavy ion collisions will be compared with that in proton induced reactions where no QGP formation is expected.

In relativistic heavy-ion collisions lots of strange particles (kaons and hyperons) are produced, offering a unique possibility to create exotic nuclear objects with strangeness - hypernuclei [5]. The energy range of the NICA research program covers the region of the maximal baryon density where the production rates of nuclear clusters with strangeness are predicted to be enhanced considerably: as many as $3 \cdot 10^{-2}$ of ${}^3_{\Lambda}\text{H}$ and $1 \cdot 10^{-5}$ of ${}^5_{\Lambda\Lambda}\text{He}$ per unit of rapidity are expected in a central Au+Au collision at $\sqrt{s} = 5$ A GeV [6]. With a typical event rate of 6 kHz for the design NICA luminosity of $10^{27} \text{ cm}^{-2} \text{ c}^{-1}$ a detailed study of the production mechanism of single hypernuclei as well as an observation of double hypernuclei at NICA look feasible.

The goal of this study was to evaluate the performance of the MPD detector for reconstruction of hyperons and hypertriton in Au+Au collisions.

2. Detector MPD

The detector for exploring the phase diagram of strongly interacting matter in a high track multiplicity environment has to cover a large phase space, be functional at high interaction rates and comprise high efficiency and excellent particle identification capabilities. The MPD detector, shown in Fig. 1, matches all these requirements. The detailed description of the MPD geometry can be found in Refs. [2, 4]. Its main tracker is the time projection chamber (TPC) supplemented by the inner tracker (IT). IT and TPC have to provide precise tracking, momentum determination and vertex reconstruction. The time of flight (TOF) system must be able to identify charged hadrons and nuclear clusters in a broad pseudorapidity range. The electromagnetic calorimeter (ECal) should identify electrons and photons and measure their energy with high precision. The zero degree calorimeter (ZDC) should provide event centrality and event plane determination and measure-

ment of the energy deposited by spectators. There are also an endcap straw-tube tracker (ECT), cathode pad chambers (CPC) and gas electron multiplier (GEM) detectors for particle tracking in the forward-backward region and a forward detector (FD) for event triggering and generating start pulse for TOF detector.

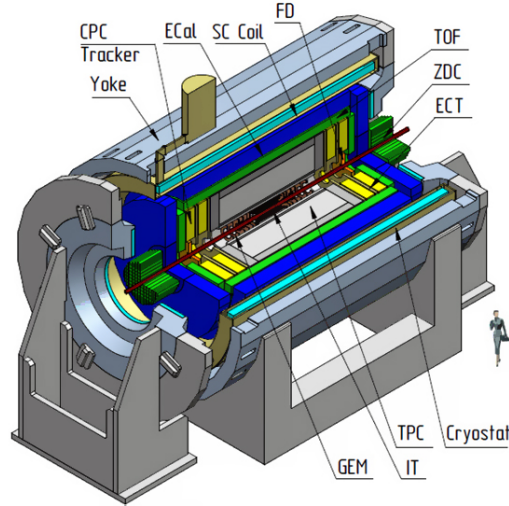


Figure 1: MPD geometry

3. Event generators and data sets

The hyperon study was done using event samples of central Au-Au collisions ($0 - 3.0$ fm) at $\sqrt{s} = 9A$ GeV produced with the UrQMD [7] generator. The number of events ranged from 10^4 to $3 \cdot 10^5$. The event sample of $5 \cdot 10^5$ central ($0 - 3.8$ fm) Au-Au collisions for hypernuclei studies has been produced with the DCM-QGSM (Dubna Cascade Model – Quark-Gluon String Model) generator [8, 9, 10] at $\sqrt{s} = 5A$ GeV. This choice was motivated by the fact that the DCM-QGSM event generator can produce nuclear clusters via the coalescence mechanism and describe hypernuclei yield in NICA energy region.

Particles produced by the event generators were transported through the detector using the GEANT3 transport package. The decay properties of hypernuclei (modes and branching ratios) have been introduced into GEANT from Ref. [11] (Tab. 1) and the lifetime has been taken to be the same as of Λ -hyperon.

4. Detector performance

The present analysis is based on the so-called start version of MPD, which includes TPC and barrel TOF and covers the mid-rapidity region $|\eta| < 1.3$. It should be noted here that the overall detector material budget is dominated by the contribution from the TPC inner and outer cages which are multilayer structures made of composite materials like kevlar and tedlar with high strength and long radiation length. As a result, the total amount of the material does not exceed 10% of the radiation length in the region of interest.

Decay channel	Branching ratio, %
$\pi^- + {}^3\text{He}$	24.7
$\pi^0 + {}^3\text{H}$	12.4
$\pi^- + \mathbf{p} + \mathbf{d}$	36.7
$\pi^0 + \mathbf{n} + \mathbf{d}$	18.4
$\pi^- + \mathbf{p} + \mathbf{p} + \mathbf{n}$	1.5
$\pi^0 + \mathbf{n} + \mathbf{n} + \mathbf{p}$	0.8
$\mathbf{d} + \mathbf{n}$	0.2
$\mathbf{p} + \mathbf{n} + \mathbf{n}$	1.5

Table 1: ${}^3\Lambda$ H decay modes and branching ratios. The studied ones are marked in bold.

4.1 Track reconstruction

The track reconstruction method is based on the Kalman filtering technique (see, e.g. [12]) and the number of TPC points per track was required to be greater than 10 to ensure a good precision of momentum and dE/dx measurements. The track finding efficiency in TPC for primary and secondary tracks is shown in Fig. 2 (left) as a function of the track transverse momentum. The secondary track sample there included particles produced within 50 cm of the primary vertex both in transverse and longitudinal directions and did not include electrons and positrons from the photon conversion. The transverse momentum resolution as a function of p_T can be seen in Fig. 2 (right). The result was obtained with the assumption on the TPC coordinate resolution of 0.5 and 1.0 mm in transverse and longitudinal directions, respectively. One can see, that the proposed detector configuration should provide the ability to efficiently reconstruct tracks with p_T above 100 MeV/c with momentum resolution below 3% (for $p_T = 0.1 - 1.5$ GeV/c).

Figure 3 (left) shows the transverse and longitudinal position uncertainties of primary tracks at their point of the closest approach to the interaction point versus track momentum. These detector characteristics are important for secondary vertex reconstruction. Both the primary and secondary vertex reconstruction methods utilized make use of the similar approach based on the Kalman filtering formalism [13]. The primary vertex reconstruction errors as functions of the track multiplicity in the event are shown in Fig. 3 (right). The primary vertex localization accuracy achieved in central Au-Au collisions is ~ 0.1 mm.

For all the reconstructed in the TPC tracks the specific energy loss dE/dx is calculated as a truncated mean of the charges of TPC hits assigned to the tracks. The truncation level of 70% was chosen, i.e. 30% of hits with the highest charges were excluded from the mean value. Next, the TPC reconstructed tracks are extrapolated to the TOF detector and matched to the TOF hits. For the matched candidates the mass square (M^2) is derived through the relation:

$$M^2 = (p/q)^2 \left(\frac{c^2 t^2}{l^2} - 1 \right)$$

where p is the track momentum, q is its charge, t is the time-of-flight from TOF, l is the path length from the collision vertex to the TOF hit, and c is the speed of light. p/q , so-called magnetic rigidity, is the value directly returned by the track reconstruction algorithm. For particles with the unit charge it is equal to the momentum and M^2 corresponds to the particle mass squared. For

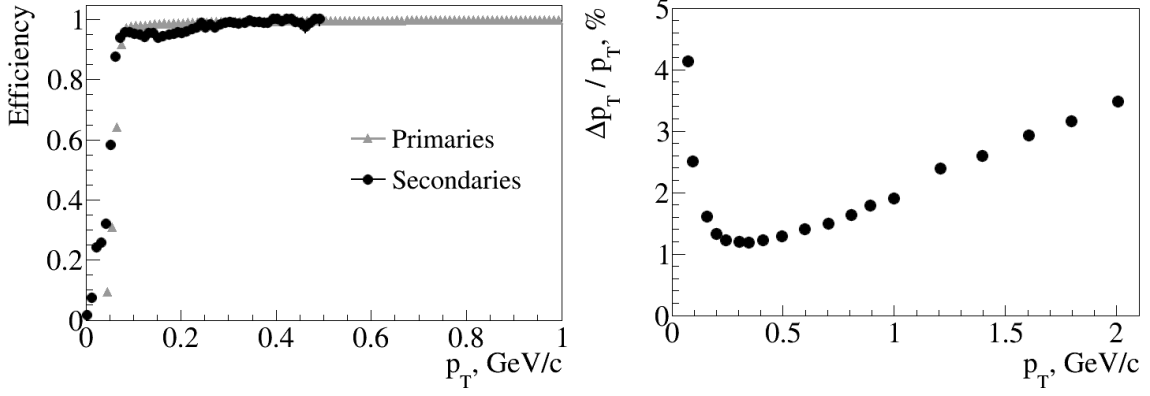


Figure 2: Left – track reconstruction efficiency as a function of track p_T for primary and secondary particles; right – relative transverse momentum resolution for primary tracks with $|\eta| < 1.3$ reconstructed in TPC.

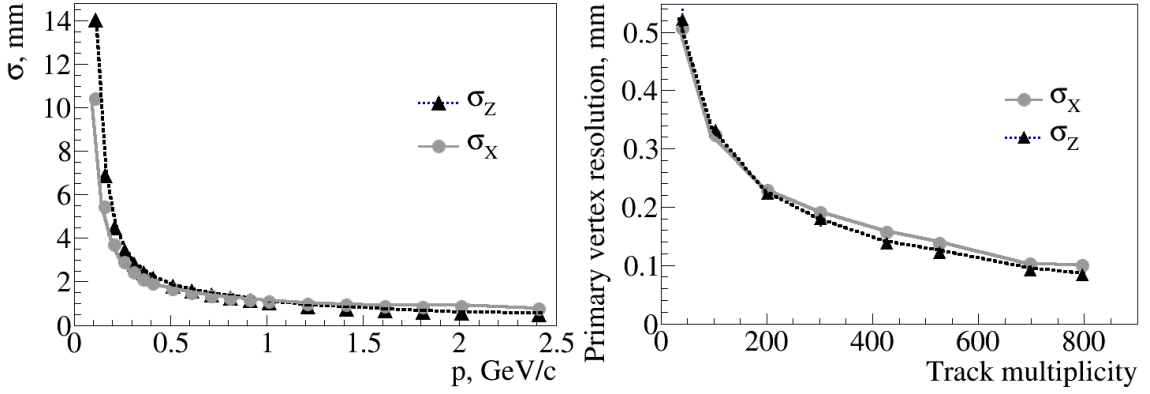


Figure 3: Left – transverse and longitudinal position errors in the point of the closest approach (PCA) to the interaction point for TPC reconstructed primary tracks with $|\eta| < 1.3$ versus particle momentum; right – transverse and longitudinal position errors of the reconstructed primary vertex as functions of the track multiplicity.

multiple-charged particles the obtained value M^2 is scaled by the factor of $1/q^2$ with respect to the true mass as can be seen, e.g., in Fig. 5 for ${}^3_\Lambda\text{He}$ (factor of $1/4$ with respect to the expected squared mass of 9).

4.2 Particle identification

Particle identification (PID) in the MPD experiment will be achieved using the energy loss (dE/dx) information from the TPC. As shown in Fig. 4 we can discriminate kaons from pions up to momenta of 0.7 GeV/c and protons can be distinguished from π , K -mesons up to $p \approx 1.3$ GeV/c. Charged particles are selected if their dE/dx measurement lies within a 3σ interval around the predicted value which is taken from the Bethe-Bloch parameterization for the mean energy loss [14].

Particles within the pseudorapidity range $|\eta| < 1.1$ can be identified using the combined time-of-flight information from the TOF detector and the dE/dx signal from TPC. Fig. 5 (left) shows a

typical dE/dx versus M^2 distribution for tracks with momentum $p = 1.5$ GeV/c.

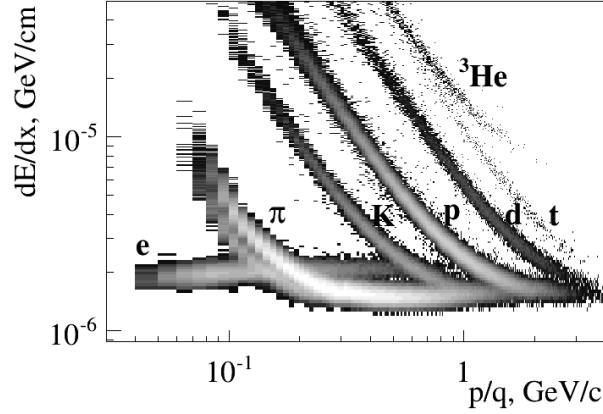


Figure 4: Specific energy loss dE/dx versus magnetic rigidity p/q for e , π , K , p , d , t , ${}^3\text{He}$.

Selected hadron and light nuclei candidates fall within the 3σ ellipses around the nominal position for a given particle type. In addition, the probability for a given particle to belong to each of the species can be calculated knowing the widths of the corresponding distributions (along the dE/dx and M^2 axes) and the difference from the predicted position for the specie. It was found that by requiring this probability to be greater than 0.75 one can get the efficiency and contamination distributions shown on Fig. 5 (right). The PID efficiency is defined as a ratio of correctly tagged to the total number of generated particles. The contamination is determined as the number of incorrectly tagged particles divided by the number of correctly tagged particles.

As seen from Fig. 5, the overall PID efficiency for p , d and ${}^3\text{He}$ is close to 100%, while due to a partial overlap of the distributions for pions and kaons the efficiency of π drops down to ≈ 0.8 at $p = 2.5$ GeV/c. The contamination of wrongly identified pions (basically from μ , e , and K) does not exceed 10%. For other species the observed contribution from mis-identified particles is negligible.

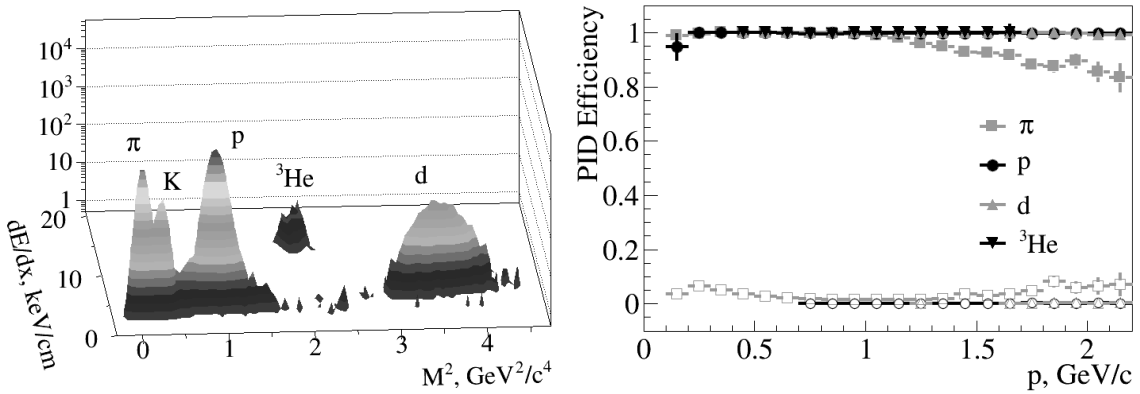


Figure 5: Left – specific energy loss dE/dx versus M^2 for π , K , p , d , ${}^3\text{He}$ at $p = 1.5$ GeV/c; right – PID efficiency (filled symbols) and contamination of mis-identified particles (empty symbols) as functions of the total momentum.

5. Analysis procedure

${}^3_\Lambda\text{H}$ hypernuclei were reconstructed using their decay modes into two (2-prong ${}^3_\Lambda\text{H}$) or three (3-prong ${}^3_\Lambda\text{H}$) charged tracks. Multistrange hyperons were reconstructed using their decay modes into a charged particle and a Λ hyperon followed by Λ decay into a proton and a pion. The signal event topology (decay of a relatively long-lived particle into two or more tracks - Fig. 6) defines the selection criteria: relatively large distance of the closest approach (DCA) to the primary vertex of decay products, small track-to-track separation in the decay vertex, relatively large decay length of the mother particle. Both the DCA and two-track separation cuts should be more efficient if applied in χ^2 -space, i.e. if normalized to their respective errors.

The exact values of selection cuts were found by performing a multidimensional scan over the whole set of selection criteria with a requirement to maximize the invariant mass peak significance, defined as $S/\sqrt{S+B}$, where S and B are total numbers of signal (described by the Gaussian) and background (polynomial function) combinations inside 2σ interval around the peak position.

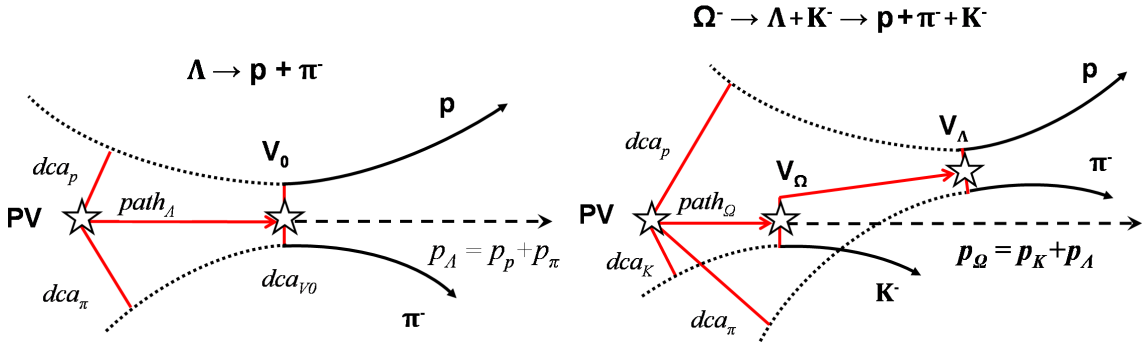


Figure 6: Left – event topology of a two-particle decay of a neutral particle (e.g. $\Lambda \rightarrow p + \pi^-$) (transverse view). Here dca_p and dca_π are the distances of the closest approach of the decay tracks to the primary vertex PV , dca_{V_0} is the distance between daughter tracks in the decay vertex V_0 , $path$ is the decay length, \mathbf{p}_p and \mathbf{p}_π are the momenta of daughter particles. ${}^3_\Lambda\text{H}$ -decays look similar except the mother particle trajectory which is a curved line, and there is a third daughter particle in 3-prong decays. Right – event topology of cascade-type decays (e.g. $\Omega^- \rightarrow \Lambda + K^- \rightarrow p + \pi^- + K^-$) (transverse view). Notations are similar.

6. Results and discussion

6.1 Reconstruction of Λ and $\bar{\Lambda}$ - hyperons

The results (Tab. 2 and Fig. 7) have been obtained for 10^4 (Λ) and $4 \cdot 10^4$ ($\bar{\Lambda}$) central Au+Au events from the UrQMD generator at $\sqrt{s} = 9\text{A GeV}$, corresponding to about 30 seconds and 2 minutes of data taking time. Table 2 shows the effect of the detector acceptance (i.e. η -coverage and low- p_T cut for decay products) on hyperon detection efficiency where the efficiency is defined with respect to the total number of hyperons. Lines 2-5 demonstrate the effect of the p_T -cut on the efficiency, where p_T is the true transverse momentum of the decay pion and proton. Line 6 shows the reconstruction efficiency, i.e. considering the reconstructed in the detector decay pions and protons without any explicit p_T -cut (and without PID efficiency). The last line includes all the relevant factors, i.e. reconstruction and PID efficiencies as well as selection efficiency. One can

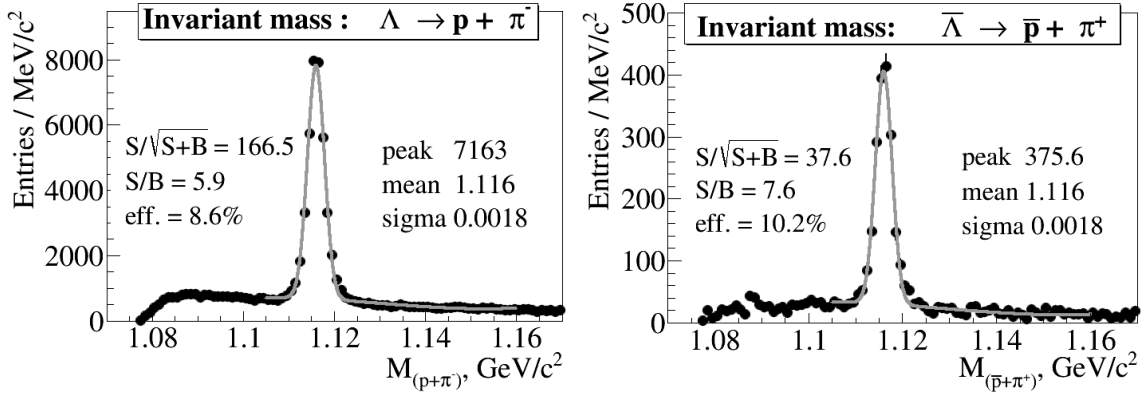


Figure 7: Reconstructed invariant mass of proton (antiproton) and π^- (π^+).

see that the detector provides efficient reconstruction of hyperons with p_T of decay tracks above 0.1 GeV/c in good agreement with Fig. 2. It is clear also that a higher p_T -threshold (e.g. 0.2 GeV/c) would significantly reduce the detector efficiency. The efficiency drop due to selection cuts comes from the necessity to suppress the combinatorial background in order to obtain a clean invariant mass peak.

The peaks of Λ and $\bar{\Lambda}$ are clearly seen and in spite of a much lower production rate for anti-lambdas relative to the one for Λ ($\bar{\Lambda}/\Lambda \approx 10^{-2}$ in central Au+Au at $\sqrt{s} = 9$ GeV), the obtained results for both the selection and total efficiencies are better than those for Λ (see Tab. 2). This is due to a higher fraction of antiprotons from weak decays in the total \bar{p} sample as compared to the proton case.

6.2 Reconstruction of Ξ^- and Ω^- - hyperons

The results (Tab. 3 and Fig. 8) have been obtained for $4 \cdot 10^4$ (Ξ^-) and $3 \cdot 10^5$ (Ω^-) central Au+Au events from the UrQMD generator at $\sqrt{s} = 9$ A GeV, corresponding to about 2 and 17 minutes of running time at the NICA collision rate of 6 kHz. Here, Λ -candidates in the invariant mass interval $\pm 3\sigma$ around the peak position were combined with negative pions (kaons) to form Ξ^- (Ω^-) - candidates. In the selection procedure, additional acceptance cuts were introduced to find the significance maximum for this cascade decay topology.

Factor	Efficiency, %	
	Λ	$\bar{\Lambda}$
Branching ratio: $\Lambda \rightarrow p + \pi^-$ ($\bar{\Lambda} \rightarrow \bar{p} + \pi^+$)	63.4	63.5
p and π^- at $ \eta < 1.3$	29.9	35.1
p and π^- at $ \eta < 1.3$ and $p_T > 0.05$ GeV/c	28.3	32.9
p and π^- at $ \eta < 1.3$ and $p_T > 0.1$ GeV/c	22.0	26.0
p and π^- at $ \eta < 1.3$ and $p_T > 0.2$ GeV/c	8.6	10.3
Reconstructed p and π^- at $ \eta < 1.3$	22.7	26.5
Maximum significance	8.6	10.3

Table 2: Factors affecting Λ ($\bar{\Lambda}$) reconstruction efficiency.

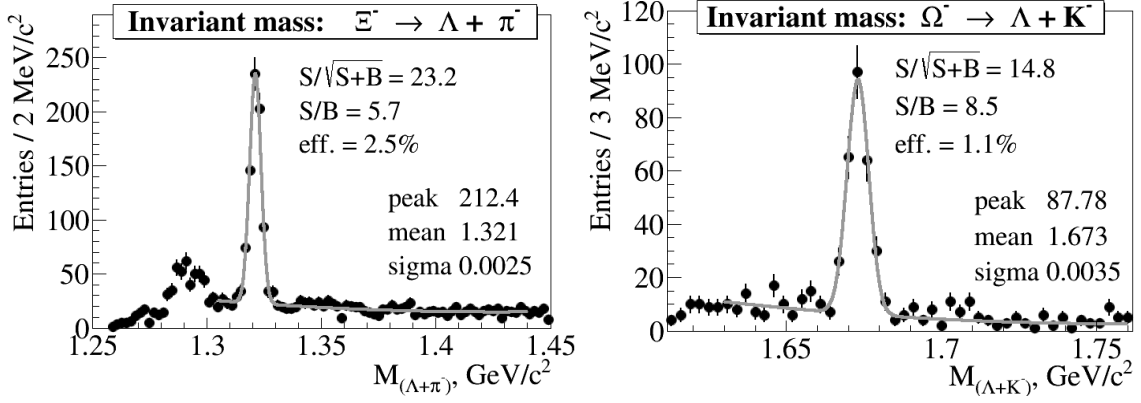


Figure 8: Reconstructed invariant mass of Λ candidate and π^- (K^-).

Here the necessity of suppressing a larger combinatorial background and a requirement to have a sufficient significance of the signal resulted in stronger cuts and lower efficiencies. Also, as in the case of lighter hyperons, we observed a large drop in the overall reconstruction efficiency when the low- p_T cut-off of decay products was increased from 0.1 to 0.2 GeV/c. Therefore, the MPD detector's ability of reconstructing very low momentum particles (at least, down to $p_T = 0.1$ GeV/c) is of crucial importance for measurements of multistrange hyperons.

6.3 Reconstruction of hypernuclei

The results (Fig. 9 and Tab. 4) have been obtained for $5 \cdot 10^5$ central Au+Au events with DCM-QGSM generator at $\sqrt{s} = 5A$ GeV, corresponding to about 30 minutes of data taking time at NICA. Figure 9 shows invariant mass distributions for 2-prong (${}^3_\Lambda\text{H} \rightarrow {}^3\text{He} + \pi^-$) and 3-prong (${}^3_\Lambda\text{H} \rightarrow p + d + \pi^-$) decay modes. Here it was necessary to suppress a larger combinatorial background as compared to the previous cases, and the requirement to have a sufficient significance of the signal resulted in stronger cuts and much lower efficiencies. Also, we observed a much larger drop in the overall reconstruction efficiency for hypertritons as compared to Λ hyperons (Tabs. 2) when the low- p_T cut-off of decay products was increased from 0.1 to 0.2 GeV/c. Therefore, as in the case of multistrange hyperons, the MPD detector's ability to reconstruct very low momentum particles (at least, down to $p_T = 0.1$ GeV/c) is of crucial importance for measurements of hypernuclei.

Factor	Efficiency, %	
	Ξ^-	Ω^-
Branching ratio: $\Xi^- (\Omega^-) \rightarrow \Lambda + \pi^- (K^-)$ ($\Lambda \rightarrow p + \pi^-$)	63.6	42.8
p, π^- and $\pi^- (K^-)$ at $ \eta < 1.3$	27.2	18.4
p, π^- and $\pi^- (K^-)$ at $ \eta < 1.3$ and $p_T > 0.05$ GeV/c	24.6	17.2
p, π^- and $\pi^- (K^-)$ at $ \eta < 1.3$ and $p_T > 0.1$ GeV/c	15.0	12.2
p, π^- and $\pi^- (K^-)$ at $ \eta < 1.3$ and $p_T > 0.2$ GeV/c	2.9	3.6
Reconstructed p, π^- and $\pi^- (K^-)$ at $ \eta < 1.3$	16.3	10.0
Maximum significance	2.5	1.1

Table 3: Factors affecting Ξ^- (Ω^-) reconstruction efficiency.

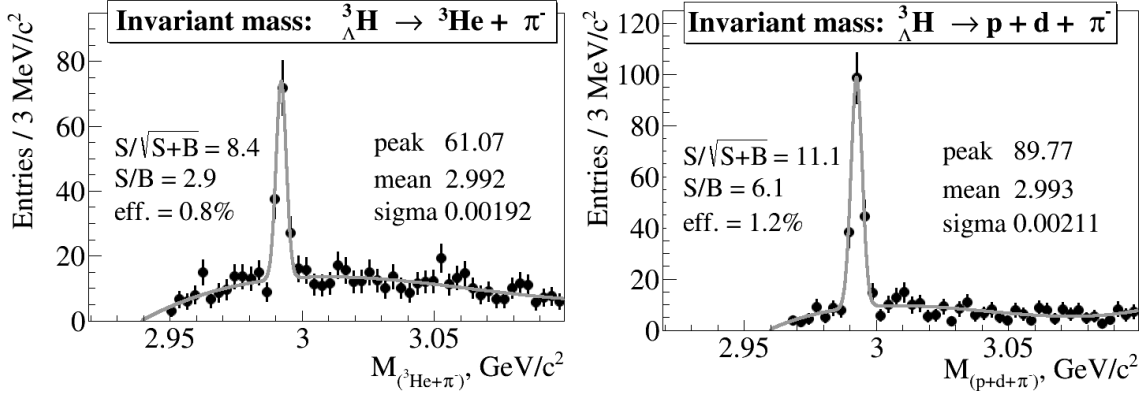


Figure 9: Left – reconstructed invariant mass of ${}^3\text{He}$ and π^- ; right – reconstructed invariant mass of proton, deuteron and π^- .

Factor	Efficiency, %	
	2-prong decay	3-prong decay
Branching ratio	24.6	36.4
Decay products at $ \eta < 1.3$	14.9	19.8
Decay products at $ \eta < 1.3$ and $p_T > 0.05$ GeV/c	14.2	15.7
Decay products at $ \eta < 1.3$ and $p_T > 0.1$ GeV/c	8.9	6.2
Decay products at $ \eta < 1.3$ and $p_T > 0.2$ GeV/c	0.7	0.1
Reconstructed decay products at $ \eta < 1.3$	7.9	8.3
Maximum significance	0.8	1.2

Table 4: Factors affecting ${}^3\Lambda\text{H}$ reconstruction efficiency.

Particle	Λ	$\bar{\Lambda}$	Ξ^-	Ω^-	${}^3\Lambda\text{H}$
Expected yield	$5.8 \cdot 10^9$	$7.3 \cdot 10^7$	$2.9 \cdot 10^7$	$1.4 \cdot 10^6$	$9.1 \cdot 10^5$

Table 5: Expected particle yields in central Au+Au collisions for 10 weeks of running time.

7. Summary

We have performed a simulation study of the MPD detector capabilities to reconstruct hyperons (Λ , $\bar{\Lambda}$, Ξ^- and Ω^-) in central Au+Au collisions at $\sqrt{s} = 9\text{A}$ GeV and hypertritons ${}^3\Lambda\text{H}$ at $\sqrt{s} = 5\text{A}$ GeV. The UrQMD and DCM-QGSM event generators were used as the input for the study of the MPD detector set-up comprising the Time Projection Chamber and barrel Time-Of-Flight system. Particle identification was achieved by combining the energy loss (from TPC) and time-of-flight (from TOF) measurements. A special procedure aimed at the maximization of the significance of the reconstructed invariant mass was developed resulting in the observed signal-to-background ratio $S/B \gtrsim 6$ for hyperons and $S/B = 3 - 6$ for hypertritons. The invariant mass resolution of ≈ 3 MeV/c² for multistrange hyperons and ≈ 2 MeV/c² for hypertriton has been achieved. Based on the results of this study and model predictions, we have estimated the expected yield of particle species under interest for 10 weeks of data taking (see Table 5). It is planned to develop a

reconstruction algorithm for double-strange nuclei ${}^4_{\Lambda\Lambda}\text{H}$ and ${}^5_{\Lambda\Lambda}\text{He}$.

References

- [1] <http://nica.jinr.ru>.
- [2] [http://nica.jinr.ru/files/CDR MPD/MPD CDR en.pdf](http://nica.jinr.ru/files/CDR_MPD/MPD_CDR_en.pdf).
- [3] J. Rafelski and B. Mülle, *Strangeness Production in the Quark-Gluon Plasma*, *Phys. Rev. Lett.* **48**, 1066 (1982).
- [4] K. U. Abraamyan et al., *The MPD detector at the NICA heavy-ion collider at JINR*, *Nucl. Instrum. Meth. A*, **628**, 99 (2011).
- [5] A. K. Kermann and M.S. Weiss, *Superstrange Nuclei*, *Phys. Rev. C*, **8**, 408 (1973).
- [6] A. Andronic, P. Braun-Munzinger, J. Stachel and H. Stöcker, *Production of light nuclei, hypernuclei and their antiparticles in relativistic nuclear collisions*, *Phys. Lett. B*, **697**, 203 (2011).
- [7] <http://urqmd.org/>.
- [8] V. D. Toneev and K.K. Gudima, *Particle Emission In Light And Heavy Ion Reactions*, *Nucl. Phys. A*, **400**, 173 (1983).
- [9] V. D. Toneev, N. S. Amelin, K. K. Gudima and S. Y. Sivoklov, *Dynamics of relativistic heavy ion collisions*, *Nucl. Phys. A*, **519**, 463 (1990).
- [10] N. S. Amelin, K. K. Gudima, S. Y. Sivoklov and V. D. Toneev, *Further Development of a Quark-Gluon String Model for Describing High-energy Collisions With a Nuclear Target*, *Sov. J. Nucl. Phys.*, **52**, 272 (1990).
- [11] H. Kamada, J. Golak, K. Miyagawa, H. Witala and W. Gloeckle, *Pi mesonic decay of the hypertriton*, *Phys. Rev. C*, **57**, 1595 (1998).
- [12] R. Frühwirth, *Application of Kalman filtering to track and vertex fitting*, *Nucl. Instr. and Meth. A*, **262**, 444 (1987).
- [13] R. Luchsinger and Ch. Grab, *Vertex reconstruction by means of the method of Kalman filter*, *Comp. Phys. Comm.*, **76**, 263 (1993).
- [14] J. Beringer et al. (Particle Data Group), *Review of Particle Physics (RPP)*, *Phys. Rev. D*, **86**, 010001 (2012).